

1     **Impacts of the January 2022 Tonga volcanic eruption on**  
2             **the ionospheric dynamo: ICON-MIGHTI and Swarm**  
3             **observations of extreme neutral winds and currents**

4     **Brian J. Harding<sup>1</sup>, Yen-Jung Joanne Wu<sup>1</sup>, Patrick Alken<sup>2</sup>, Yosuke Yamazaki<sup>3</sup>,**  
5     **Colin C. Triplett<sup>1</sup>, Thomas J. Immel<sup>1</sup>, L. Claire Gasque<sup>1</sup>, Stephen B. Mende<sup>1</sup>,**  
6             **Chao Xiong<sup>4</sup>**

7             <sup>1</sup>Space Sciences Laboratory, University of California Berkeley, Berkeley, CA, USA

8             <sup>2</sup>University of Colorado, Boulder, CO, USA

9             <sup>3</sup>GFZ German Research Centre for Geosciences, Potsdam, Germany

10            <sup>4</sup>Department of Space Physics, Electronic Information School, Wuhan University, 430072 Wuhan, China

11            **Key Points:**

- 12            • Extreme thermospheric winds and ionospheric currents were observed in coordi-  
13            nated space/ground-based measurements, ten hours post-eruption
- 14            • The westward electrojet current when the Lamb wave reaches the dayside is con-  
15            sistent with recent studies of the wind-driven electrojet
- 16            • Observations of linked dynamo processes provide direct evidence of the space-weather  
17            impacts of acute lower atmospheric forcing

## 18 Abstract

19 The eruption of the Hunga Tonga-Hunga Ha’apai volcano on 15 January 2022 dis-  
 20 turbed the atmosphere at all altitudes. The NASA Ionospheric Connection Explorer (ICON)  
 21 and ESA Swarm satellites were well placed to observe its impact on the ionospheric wind  
 22 dynamo. After the lower atmospheric wave entered the dayside, Swarm A observed an  
 23 eastward and then westward equatorial electrojet (EEJ) on two consecutive orbits, each  
 24 with magnitudes exceeding the 99.9th percentile of typical variation. ICON simultane-  
 25 ously observed the neutral wind (90–300 km altitude) at approximately the same dis-  
 26 tance from Tonga. The observed neutral winds were also extreme (>99.9th percentile  
 27 at some altitudes). The covariation of EEJ and winds is consistent with recent theoret-  
 28 ical and observational results, indicating that the westward electrojet is driven by a strong  
 29 westward Pedersen-region wind. This result confirms that the eruption not only created  
 30 small-scale waves in the thermosphere-ionosphere but also caused unprecedented large-  
 31 scale electrodynamic modifications.

## 32 Plain Language Summary

33 The January 2022 Tonga volcanic eruption caused atmospheric impacts around the  
 34 world. As a natural experiment, it can be used to test our understanding of how the lower  
 35 atmosphere affects space weather. Researchers are only beginning to document the chain  
 36 of events post-eruption, and this paper focuses on its impact on the generator that drives  
 37 electric fields in near-Earth space, a key part of space weather. This generator is driven  
 38 by the atmosphere pushing charged particles across Earth’s magnetic field. This usually  
 39 creates a strong eastward current above the equator. When the Swarm A satellite co-  
 40 incided with the wave from Tonga, it observed that this current strengthened dramati-  
 41 cally, then reversed. Although reversals are not unusual, this was the strongest rever-  
 42 sal observed by Swarm since its 2013 launch, except for one large geomagnetic storm in  
 43 2015. Another satellite, the Ionospheric Connection Explorer, was luckily at the right  
 44 time and place to observe related motions of the upper atmosphere, which were similarly  
 45 extreme. These observations are shown to be consistent with our theoretical understand-  
 46 ing of the generator. This study is important because it represents a critical test of atmo-  
 47 sphere-space interactions and implies that the Tonga eruption was a major space weather event.

## 48 1 Introduction

49 Isolated disturbances such as earthquakes, tsunamis, and solar eclipses, as well as  
 50 explosions from volcanoes, nuclear detonations, and meteor air bursts can offer discrete  
 51 tests for models of atmosphere-ionosphere coupling and variability (Aryal et al., 2020;  
 52 Astafyeva, 2019; Inchin, Snively, et al., 2020; Li et al., 2021; Zettergren & Snively, 2019).  
 53 The Hunga Tonga-Hunga Ha’apai (hereafter Tonga) volcanic eruption on 15 Jan 2022  
 54 generated atmospheric disturbances from the ground to the ionosphere (Adam, 2022; Jet  
 55 Propulsion Laboratory, 2022). Tropospheric and stratospheric observations reported the  
 56 presence of a Lamb wave propagating around the globe (Duncombe, 2022). Although  
 57 the Lamb wave propagates in the troposphere with a velocity around 310 m/s (Bretherton,  
 58 1969), energy leaks into the upper atmosphere, and the amplitude of wind, temperature,  
 59 and pressure fluctuations can grow with altitude (Nishida et al., 2014). As such, the iono-  
 60 sphere, readily observed by ground-based instruments, can function as a sensitive mon-  
 61 itor of atmospheric disturbances.

62 Indeed, initial Total Electron Content (TEC) observations have reported Travel-  
 63 ing Ionospheric Disturbances (TIDs) propagating globally for many hours and even days  
 64 after the Tonga eruption (Lin et al., 2022; Themens et al., 2022; Zhang et al., 2022). Ad-  
 65 ditionally, Soares et al. (2022) reported oscillations of the geomagnetic field observed by  
 66 a ground-based magnetometer 835 km from Tonga, which are attributed to short-period

67 modulation (3-5 min) of ionospheric currents. No studies have yet reported on processes  
68 connecting the lower atmosphere with these ionospheric signatures.

69 The mechanisms through which signals from the lower atmosphere are transmit-  
70 ted and create observable effects in the ionosphere are complex, and understanding their  
71 interplay is critical for interpreting and predicting ionospheric signals. These mechanisms  
72 include those resulting from direct propagation of the wave or waves to ionospheric  $F$ -  
73 region heights, modifying ion drag and/or plasma loss rates. Another mechanism is in-  
74 direct, mediated by electric fields resulting from the neutral wind dynamo, which can  
75 carry signatures along magnetic field lines from the  $E$  region to the  $F$  region. The sig-  
76 nal can also be transmitted to the opposite hemisphere, which has been proposed to ex-  
77 plain the appearance of TIDs over Japan ahead of the Lamb wave (Lin et al., 2022). In  
78 this study we report on two aspects of the Tonga disturbance: neutral winds and iono-  
79 spheric dynamo signatures.

80 Specifically, we report extreme perturbations in the equatorial electrojet (EEJ) ob-  
81 served by Swarm and extreme perturbations in neutral winds from 90 to 300 km alti-  
82 tude observed by the Michelson Interferometer for Global High-resolution Thermospheric  
83 Imaging (MIGHTI) on the Ionospheric Connection Explorer (ICON) (Immel et al., 2018).  
84 The EEJ is an intense band of zonal current confined near the magnetic equator flow-  
85 ing in the daytime between  $\sim 90$  and 120 km altitude (Yamazaki & Maute, 2017, and ref-  
86 erences therein). Variations in the EEJ closely track those of the equatorial zonal elec-  
87 tric field (i.e., vertical plasma drift) which has widespread effects on the equatorial iono-  
88 sphere by modifying the production-loss-transport balance. Typically the EEJ flows east-  
89 ward, associated with an eastward zonal electric field, upward drift, and enhanced equa-  
90 torial fountain effect, but sometimes the EEJ flows westward, associated with the op-  
91 posite ionospheric conditions. In the absence of direct solar insolation, the EEJ disap-  
92 pears at night.

93 ICON and Swarm have been operating simultaneously since ICON's launch in 2019,  
94 offering an unprecedented observational capability for studies related to the ionospheric  
95 dynamo. On 15 Jan 2022, their orbits were unusually well-synced to provide complemen-  
96 tary observations of the Tonga signature, as discussed below. This study does not at-  
97 tempt to quantify properties or classifications of the waves excited by the Tonga explo-  
98 sion, which will undoubtedly be a focus of future investigations. However, the unique  
99 opportunity created by coincident observations of the neutral wind by MIGHTI and iono-  
100 spheric currents by Swarm allows us to directly study the impact of these waves on the  
101 ionospheric dynamo, which we report here. In addition, four magnetometer sites are uti-  
102 lized to provide a ground-based perspective on the EEJ variation.

## 103 2 Data sources

### 104 2.1 ICON-MIGHTI neutral winds

105 This study uses neutral wind data from the MIGHTI instrument on the ICON space-  
106 craft, which is in a  $27^\circ$  inclination orbit. Neutral wind profiles (ICON data product 2.2  
107 v04) from 90 to 300 km altitude are derived by remote limb observations of the Doppler  
108 shift of naturally occurring green 557.7 nm and red 630.0 nm (OI) airglow emissions. We  
109 only use wind data from the dayside, which is when the airglow layers are wide enough  
110 to permit wind estimates spanning the full 90 to 300 km altitude range, which fully en-  
111 compasses the dynamo region. Nightside data have a gap from  $\sim 109$  to 210 km. Data  
112 are available from the green and red channels with vertical sampling of  $\sim 3$  km and  $\sim 10$   
113 km, respectively. For this study, to improve statistics especially in regions of dim airglow,  
114 we preprocess the green channel by binning vertically by a factor of 2, yielding  $\sim 6$  km  
115 sampling. Below 180 km altitude, we use samples from the green channel, and above 180  
116 km, we use samples from the red channel. Data above 180 km have a negligible impact

117 on our conclusions regarding the wind dynamo but are included because the volcanogenic  
 118 waves are clearly evident up to 300 km. The reader is referred to previous publications  
 119 for more information on the MIGHTI instrument (Englert et al., 2017), processing al-  
 120 gorithms (Harding et al., 2017), and on-orbit validation (Harding et al., 2021; Makela  
 121 et al., 2021).

122 Although the focus is on two orbits on 15 Jan 2022, we also make use of the en-  
 123 tire dataset for background statistics. Specifically, we use all MIGHTI profiles from the  
 124 start of the mission until 14 Jan 2022 for which the variable “Wind\_Quality” is equal  
 125 to 1 (i.e., highest quality, 1,086,830 profiles in total). To generate these statistics, in ad-  
 126 dition to the altitude binning discussed above, the data were preprocessed with a 5-sample  
 127 median filter in time to remove outliers. Data obtained during geomagnetic storms are  
 128 included in these statistics. Statistics are presented in terms of percentiles; for example,  
 129 the 90% level for zonal wind represents a value such that 10% of samples have a zonal  
 130 wind larger than that level.

## 131 2.2 Swarm A EEJ current

132 The Swarm constellation comprises three satellites in near-polar orbits. In this study  
 133 we use EEJ intensity estimates from one spacecraft, Swarm A, which has an inclination  
 134 of 87.4°. Latitude-dependent height-integrated EEJ intensity are provided by the Swarm  
 135 Level 2 Product EEF (Eastward Electric Field) (Alken et al., 2013). The EEJ current  
 136 is estimated from magnetometer measurements during every dayside overflight of the mag-  
 137 netic equator (Alken, 2020). Ground-based validation is discussed by Alken et al. (2015).

138 In a manner analogous to the wind analysis, background statistics are calculated  
 139 for context, using the entire available dataset. Specifically, we use the version 0204 dataset  
 140 spanning 25 Nov 2013 to 14 Jan 2022. We first preprocess the EEJ data to remove non-  
 141 physical current distributions. These outliers are identified by computing the the total  
 142 “off-peak current” for each overflight (defined as the root-mean-square of currents pole-  
 143 ward of 5 deg quasidipole latitude). Overflights are removed if the off-peak current is larger  
 144 than 100 times the interquartile range of all the overflights (i.e., 75th percentile minus  
 145 25th percentile). This removes 25 overflights which are, by visual inspection, clear non-  
 146 physical outliers. The 45,184 remaining overflights are used in the statistics below. All  
 147 data on 15 Jan 2022 remain after this preprocessing step.

## 148 2.3 Ground-based magnetometers

149 We also use ground-based magnetometer data to support the interpretation of the  
 150 EEJ behavior on 15 Jan 2022. The intensity of the EEJ can be estimated using the hor-  
 151 izontal (H) component of the geomagnetic field observed at two stations, one being lo-  
 152 cated at the magnetic equator and the other located about the same longitude but out-  
 153 side the EEJ band (Anderson et al., 2004). The difference in H ( $\Delta H$ ) at the two stations,  
 154 after subtracting the nighttime baseline, represents the EEJ intensity. We use data from  
 155 Huancayo (HUA, 12.0°S, 75.3°W) and Piura (PIU, 5.2°S, 80.6°W) for the Peruvian sec-  
 156 tor, and Tatuoca (TTB, 1.2°S, 48.5°W) and Kourou (KOU, 5.2°N, 52.7°W) for the Brazil-  
 157 ian sector. These stations are positioned to detect EEJ signatures in the vicinity of the  
 158 Swarm observations.

## 159 3 Results and Discussion

### 160 3.1 Data selection and observational geometry

161 The Tonga volcanic eruption occurred around 04:15 UT on 15 Jan 2022, near lo-  
 162 cal sunset. Since the tropospheric sound speed is slower than the Earth’s rotation at these  
 163 latitudes, the Lamb wave was mostly contained to the dusk and nighttime sectors for

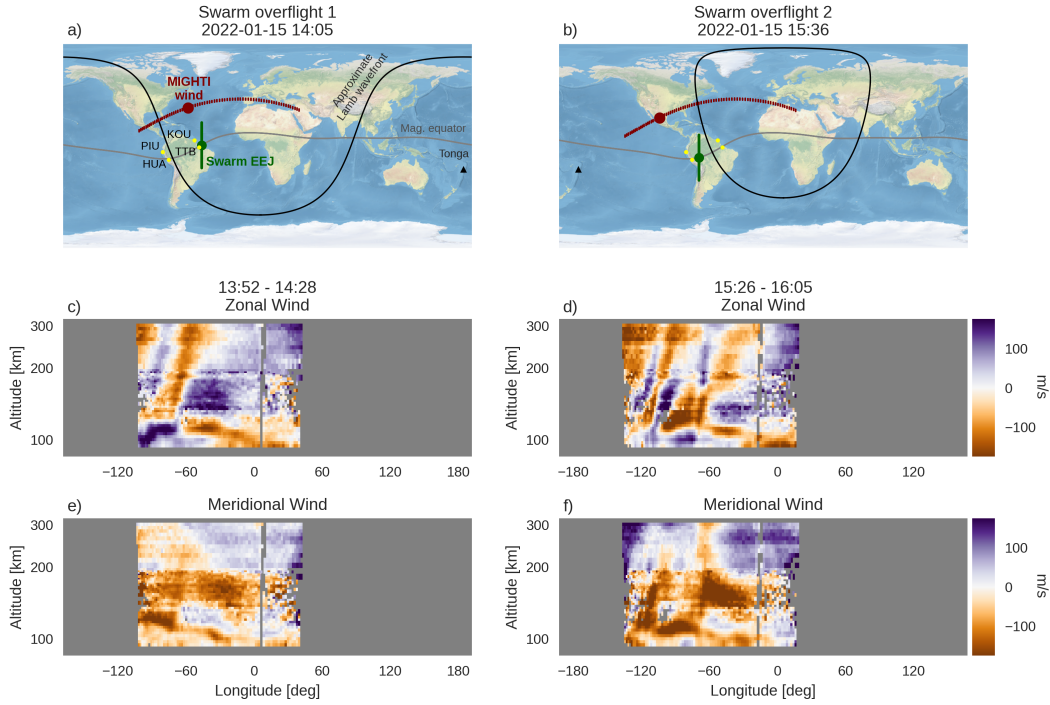


**Figure 1.** (a,b) Two consecutive orbits of ICON-MIGHTI dayside passes and Swarm equator overflights. The red and green dots indicate the location of the MIGHTI wind observation and Swarm EEJ observation at the respective time. The red and green lines indicate the observation locations just before and after this time. The dashed appearance of the red line denotes individual MIGHTI wind profile locations. The black line indicates the location of a notional radially propagating wavefront moving at 310 m/s that originated in Tonga at 04:15 UT. Although MIGHTI samples the wind  $\sim 35$  degrees farther north than the EEJ, the two sample the same great-circle distance from Tonga with a delay of several minutes. The yellow circles indicate the four ground-based magnetometer sites. (c,d) Daytime zonal wind profiles (positive eastward) measured by MIGHTI corresponding to the longitudes in the map above. Only daytime data are included. The small data gap near  $0^\circ$  longitude is caused by the quality control algorithm masking data when the moon is near the MIGHTI field of view. The altitude axis is in log scale to better display lower thermospheric winds. (e,f) Same as (c,d) for the meridional wind (positive northward).

164 the first several hours after the eruption. In this study we focus on thermosphere-ionosphere  
 165 signatures once the wave reaches the dayside, where ionospheric currents are strongest.  
 166 According to visual inspection of GOES-16/17 infrared imagery (not shown), the lower  
 167 atmospheric Lamb wave reached the dayside around 13 UT at low/mid-latitudes. The  
 168 wave reaches daylight sooner in the southern polar region, but the dynamo effects stud-  
 169 ied here occur at low latitudes, which is our focus. The Lamb wave entered the dayside  
 170 in the American longitude sector. Serendipitously, Swarm A overflights occurred in this  
 171 sector at 14:05 UT and 15:36 UT. In this study we utilize data from these two orbits and  
 172 the corresponding orbits of ICON, which samples all longitudes every orbit, albeit at dif-  
 173 ferent latitudes.

174 The two orbits of ICON-MIGHTI data are shown in Figure 1, an animated ver-  
 175 sion of which can be found in the Supporting Information (Movie S1). For context, we  
 176 show a reference 310 m/s wavefront that originated in Tonga at 04:15 UT. This value  
 177 was estimated from GOES imagery (not shown) in which the wave launched at 04:15 UT  
 178 15 Jan circled the Earth and returned to Tonga at  $\sim$ 15:40 UT on 16 Jan. This value is  
 179 not needed quantitatively, nor is it critical to our interpretation. On the first orbit (panel  
 180 a), Swarm A crossed the equator and measured the EEJ at a location roughly 3000 km  
 181 ahead of the 310 m/s wavefront. At the time Swarm A measured the EEJ at the equator,  
 182 MIGHTI sampled the wind  $\sim$ 35 degrees farther north but at a similar great-circle  
 183 distance from Tonga.

184 The next orbit is shown to the right (panel b). On this orbit, Swarm A measured  
 185 the EEJ at a location roughly 1500 km behind the assumed 310 m/s wavefront. At the  
 186 time of the Swarm A overflight, MIGHTI samples the wind roughly 3500 km behind the  
 187 wavefront, but reached the same great-circle distance as Swarm A 5 minutes later (15:41  
 188 UT).

189 In both orbits, the MIGHTI data (panels c, d, e, and f) show large wind fluctua-  
 190 tions, coherent wave structures, and vertical shears, both ahead of and behind the 310  
 191 m/s wavefront. It is apparent from these observations that the thermospheric signatures  
 192 of this event are complex and likely not explained by a single wave mode. We do not com-  
 193 ment further on the wind features in this paper, but instead we focus on their impact  
 194 on ionospheric currents in the next section.

195 In the meridional wind, a discontinuity is evident at 180 km where data from the  
 196 green and red channels are spliced together. This is a known artifact caused by a drift  
 197 in the zero-wind reference in the MIGHTI v04 dataset; a new calibration has been im-  
 198 plemented and will appear in the next version of the MIGHTI wind dataset. This dis-  
 199 continuity does not affect the qualitative conclusions of this study, which focus on the  
 200 zonal wind, nor the quantitative calculations in this study, which uses perturbations from  
 201 the mean, as described below.

### 202 3.2 Comparison between MIGHTI winds and Swarm EEJ

203 Figure 2 compares the Swarm A EEJ observations with the MIGHTI wind obser-  
 204 vations on these two orbits. On the first orbit (panel a), Swarm A observed an extremely  
 205 strong eastward EEJ (0.22 A/m). This represents the strongest EEJ observed by Swarm  
 206 A since 2017, and the 19th strongest overall (stronger than 99.96% of all observations  
 207 in the Swarm A dataset, which started in 2013). On the next orbit (panel b), Swarm A  
 208 observes an extreme westward EEJ (-0.17 A/m), often referred to as a counter-electrojet.  
 209 Except for three overflights during the 22-23 June 2015 geomagnetic storm, this repre-  
 210 sents the strongest westward EEJ in the Swarm A dataset. Swarm A data from earlier  
 211 orbits on this day do not show variations above the 90% level. Also shown are statistics  
 212 computed from all EEJ observations from the start of the mission until 14 Jan 2022. The  
 213 black line is the median, the dark gray shaded region is the interquartile range (25–75%),  
 214 and other percentile ranges are shown in lighter gray. Although Swarm B is not included

215 in this quantitative analysis, data from Swarm B also show a large positive EEJ (0.20  
 216 A/m) followed by a large negative EEJ (-0.14 A/m) on these two orbits (not shown). Swarm  
 217 C flies in a side-by-side configuration to Swarm A, and recorded similar measurements  
 218 on these two orbits (0.22 A/m and -0.17 A/m respectively, not shown).

219 The bottom of Figure 2 (panels c and d) shows the MIGHTI zonal winds correspond-  
 220 ing to the Swarm A EEJ observations, compared with background variability shown with  
 221 statistical ranges in gray, analogous to panels a and b. Although the meridional wind  
 222 fluctuations are in some cases quite significant, we focus on zonal winds because (1) merid-  
 223 ional winds are nearly parallel to the magnetic field at the equator and are not expected  
 224 to strongly influence the EEJ, and (2) the wave is propagating nearly zonally in this re-  
 225 gion, so the dominant large-scale signature of the wave is expected to be in the zonal wind.  
 226 A separate analysis was conducted where the zonal and meridional winds were combined  
 227 to calculate the radial wind perturbation in the direction away from Tonga. However,  
 228 this yielded identical conclusions and was more complicated to compare quantitatively  
 229 with background statistics.

230 Zonal wind profiles are chosen such that their distance from Tonga is identical to  
 231 Swarm A's distance when it crossed the magnetic equator. Insofar as the wave can be  
 232 assumed to propagate concentrically, this is a proxy for the neutral wind fluctuations in  
 233 the equatorial region during the Swarm A overflight. The various profiles in Figure 2 are  
 234 chosen to provide exact alignment for assumed wave velocities spanning from 300 to 330  
 235 m/s. The qualitative similarity of these profiles suggests that this procedure to align the  
 236 Swarm and MIGHTI observations is not significantly sensitive to the assumed wave ve-  
 237 locity, a consequence of the fortunate timing of the two observations. The temporal off-  
 238 sets required are 0-4 minutes (overflight 1) and 5-8 minutes (overflight 2), a time scale  
 239 that is not likely of importance for the large-scale waves observable by MIGHTI. Fur-  
 240 thermore, it is the same magnitude as the assumption of temporal persistence used to  
 241 produce the vector wind estimate by combining the data from the two MIGHTI sensors  
 242 (5-9 minutes) (Harding et al., 2017). A possibly non-negligible uncertainty in this pro-  
 243 cedure is the assumption of concentric wave propagation, as the two observations sam-  
 244 ple along different wave azimuths from Tonga, separated by 5-32 degrees.

245 The wind profiles on both orbits are extreme, showing values comparable with, or  
 246 stronger than, the 0.1% and 99.9% levels. At  $\sim 140$  km, this event produced the strongest  
 247 winds observed since the start of the mission. On orbit 1, when the EEJ is strongly east-  
 248 ward, MIGHTI observes a westward perturbation in the upper Hall region ( $\sim 100$ - $120$   
 249 km) and an eastward perturbation in the Pedersen region ( $\sim 120$ - $150$  km). On orbit 2,  
 250 when the EEJ is strongly westward, MIGHTI observes an eastward perturbation, peak-  
 251 ing around 100 km in the lower Hall region, and a westward perturbation above  $\sim 110$   
 252 km, which spans the upper Hall region and the Pedersen region.

253 This correspondence between the EEJ and neutral winds is consistent with the re-  
 254 lationship developed by Yamazaki et al. (2014) and Yamazaki et al. (2021). The early  
 255 theoretical literature on the EEJ suggested that while height-varying local winds influ-  
 256 ence the currents outside the EEJ, they are not expected to have a significant influence  
 257 on the EEJ itself, as it is dominated by the influence of the global zonal electric field (Richmond,  
 258 1973). However, the modeling study by Yamazaki et al. (2014) predicted that winds should  
 259 have a significant role and that the EEJ should be negatively correlated with Hall-region  
 260 zonal winds and positively correlated with Pedersen-region winds. This was observation-  
 261 ally confirmed with the availability of concurrent MIGHTI and Swarm observations by  
 262 Yamazaki et al. (2021). The implicated mechanism is local generation of electric fields  
 263 which was not considered in early work: (1) in the Hall region, an eastward wind drives  
 264 eastward current, which generates a westward electric field; (2) in the Pedersen region,  
 265 an eastward wind drives upward current, which generates a downward electric field. At  
 266 the footpoint of this field line, which lies in the Hall region, the westward currents driven  
 267 by this electric field will generate an eastward electric field. Since the EEJ current flows

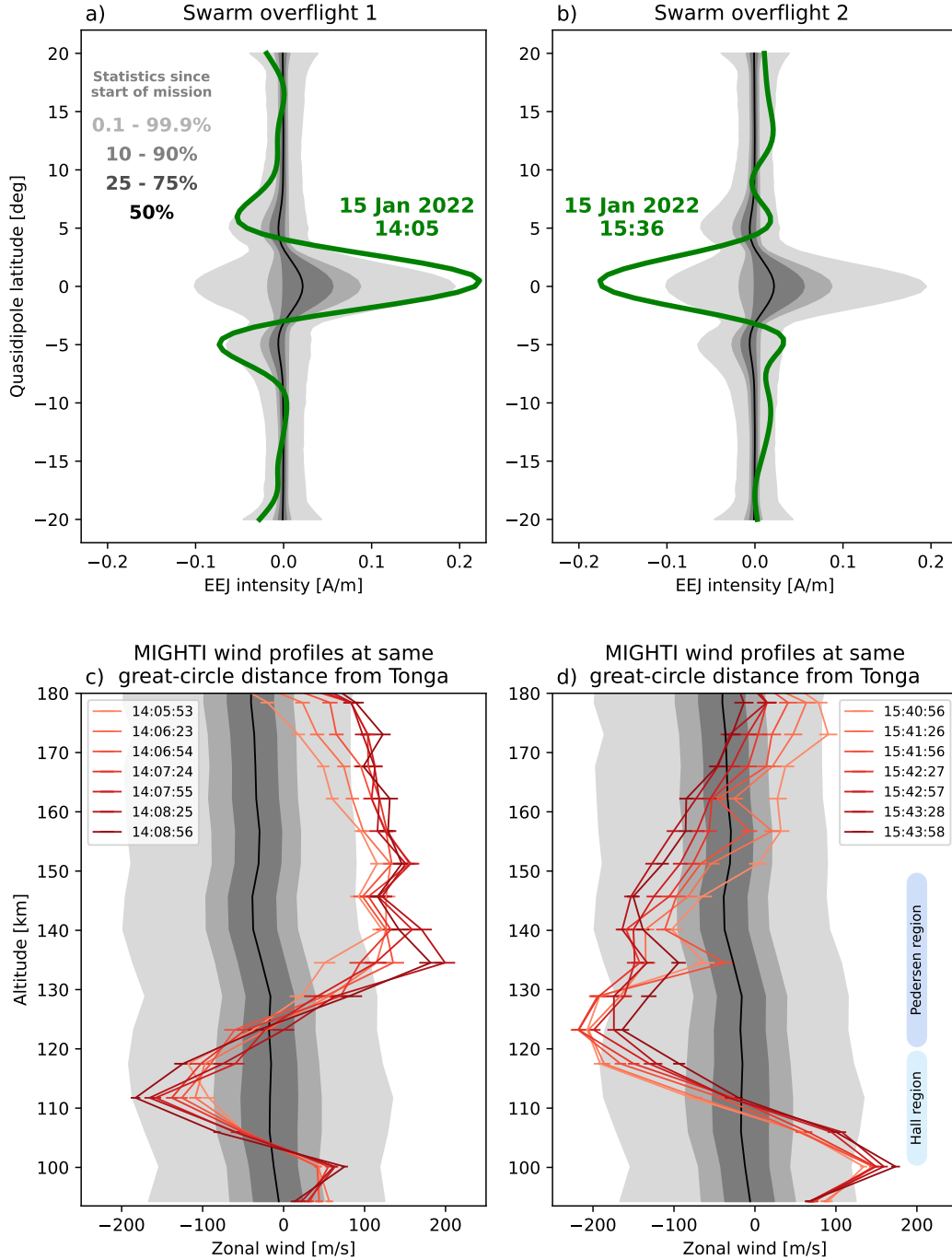


**Figure 2.** (a,b) Swarm A equatorial electrojet (EEJ) observations during the two orbits shown in Figure 1. (c) MIGHTI wind profiles during the ICON orbit contemporaneous with the Swarm overflight in panel a. (d) Same, except one orbit later, contemporaneous with the Swarm overflight in panel b. Specific wind profiles were chosen to correspond to samples at the same great-circle distance from Tonga as the Swarm observation, for various assumed wave velocities from 300 to 330 m/s. Errorbars represent the uncertainty reported in the v04 wind product, which accounts for shot, read, and dark noise in the detector (i.e., precision). In all 4 panels, the gray shaded areas represent background statistics computed from percentiles of the entire dataset from the start of each mission until 14 Jan 2022, comprising 45,184 Swarm A overflights since 25 Nov 2013 and 1,086,830 MIGHTI profiles since 6 Dec 2019. The black line is the median.

268 in the Hall region, this latter case is a noteworthy example of winds outside the EEJ per-  
 269 turbing currents in the EEJ.

270 In orbit 1, the strong westward Hall-region wind and strong eastward Pedersen-region  
 271 wind is expected to cause a strong eastward EEJ through the Yamazaki et al. (2014) re-  
 272 lationship. In orbit 2, the Hall-region wind is eastward below 110 km and westward above  
 273 110 km, which is expected to yield minimal total forcing in the Hall region. However,  
 274 the Pedersen-region wind is strongly westward, which is expected to cause a strong west-  
 275 ward EEJ. In both cases, the Swarm observations match the expectation. This result  
 276 confirms the Yamazaki relationship holds under extreme conditions. More interestingly,  
 277 because the Hall-region effect is small in orbit 2, the EEJ is apparently driven mostly  
 278 by winds at higher altitudes, confirming the importance of nonlocal wind driving of the  
 279 EEJ. The current paths that regulate this control deserve further inquiry, both obser-  
 280 vationally and theoretically.

### 281 3.3 Ground-based magnetometer data

282 In this section we report EEJ observations from two pairs of magnetometers located  
 283 near the Swarm overflights (see Figure 1). The observations are shown in the first two  
 284 panels of Figure 3 using blue lines. The black line shows the monthly mean, and the gray  
 285 shaded area represents 1 standard deviation (i.e.,  $1\sigma$ ) above and below the mean.

286 The HUA-PIU pair in Peru observes a negative  $\Delta H$  (corresponding to a westward  
 287 EEJ) beginning around 12 UT, lasting until just after 16 UT (except for one brief pe-  
 288 riod of weak eastward EEJ near 15 UT). The TTB-KOU pair in Brazil observes an east-  
 289 ward EEJ until  $\sim 15$  UT, followed by a period of westward EEJ until 18 UT. Superim-  
 290 posed on these broad patterns are shorter, 1-hour scale features which are discussed in  
 291 the next section.

292 The broad features and relative timing seen in the magnetometer data are qual-  
 293 itatively consistent with the Swarm observations. Namely, a negative disturbance is first  
 294 seen over Peru, then over Brazil 2-4 hours later, consistent with eastward propagation.  
 295 The presence of 1-hour-scale fluctuations and the lack of EEJ before sunrise makes it dif-  
 296 ficult to estimate the relative timing with greater accuracy. On the first Swarm overflight  
 297 at 14:05 UT, the nearby Brazilian pair observes an eastward EEJ which is  $1\sigma$  or less above  
 298 the climatology. On the second Swarm overflight at 15:36 UT, the Peruvian pair observes  
 299 a  $\sim 2.5\sigma$  extreme westward EEJ. Especially for the positive EEJ on overflight 1, the fluc-  
 300 tuations seen by the ground-based magnetometers are not as extreme as the Swarm ob-  
 301 servations. Although the cause of this is unknown, it could be due to the ground-based  
 302 magnetometers being slightly offset from the magnetic equator. In January 2022, TTB  
 303 and HUA were  $2.2^\circ$  and  $0.8^\circ$  off the magnetic equator according to the CHAOS 7.8 model  
 304 (Finlay et al., 2020).

305 The different temporal patterns in Peru and Brazil confirm that the fluctuations  
 306 observed by Swarm A are not purely spatial but also temporal. The ground-based mag-  
 307 netometer data suggest that the most extreme EEJ activity may have been at locations  
 308 and times not sampled by Swarm A (e.g., over Brazil at 16 UT). Future work utilizing  
 309 the global network of magnetometers could help elucidate the evolution of global cur-  
 310 rents during this event.

311 The magnetometer data show disturbances before the arrival of the 310 m/s wave-  
 312 front (e.g., the negative  $\Delta H$  in Peru at 13 UT, and the positive and negative  $\Delta H$  in Brazil  
 313 before 16 UT). This is consistent with the Swarm A observations ahead of the wavefront  
 314 at 14:05 UT (Figures 1a and 2a) and the MIGHTI observations on the first orbit (Fig-  
 315 ure 1c, eastward of  $-60^\circ$  longitude). It is likely that the thermospheric response to the  
 316 eruption is not as simple as the Lamb wave observed in the lower atmosphere, due to  
 317 the effects of nonlinear evolution, dispersion, self-acceleration, and secondary wave gen-

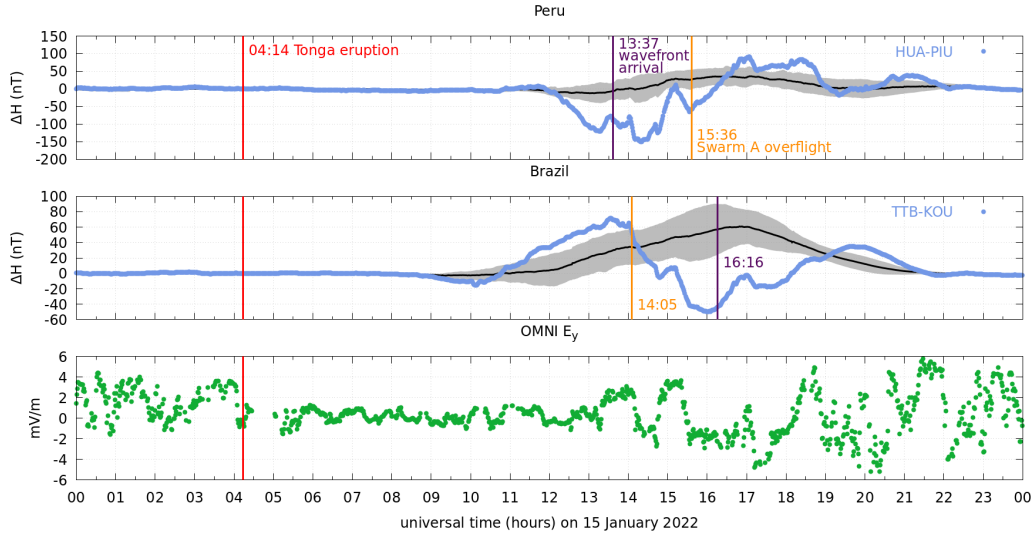


**Figure 3.** (top) Ground-based magnetometer EEJ intensity estimates over Peru on 15 Jan 2022 computed by subtracting PIU data (off-equator) data from HUA data (on-equator), shown in blue. The monthly mean is in black and  $\pm 1$  standard deviation range is in gray. The arrival time of a reference 310 m/s wavefront (purple line) and time of Swarm overflight (yellow line) are also shown. (middle) Same as top, but for Brazil (TTB - KOU). (bottom) Interplanetary eastward electric field from the OMNI database.

318 eration, among others (see Inchin, Heale, et al. (2020) for a first-principles model of the  
 319 thermospheric signature of tsunamis).

### 320 3.4 Geomagnetic storm effects

321 A moderate geomagnetic storm began on 14 Jan 2022; the Tonga eruption and sub-  
 322 sequent wave propagation occurred during the recovery phase. It is thus important to  
 323 distinguish the signatures caused by the Tonga eruption from the effects of the storm.  
 324 The EEJ is known to be modified by electric fields penetrating from the magnetosphere  
 325 and electric fields originating from the stormtime disturbance dynamo (Yamazaki & Maute,  
 326 2017, and references therein). First, we rule out penetration electric field effects.

327 Figure 3 (bottom panel) shows the interplanetary electric field (IEF) y-component  
 328 (dawn-to-dusk electric field) from OMNI data (King & Papitashvili, 2005). The data are  
 329 taken directly from the OMNI database, except they include a 17-minute delay to ac-  
 330 count for the delay between the bowshock and the ionosphere (Manoj et al., 2008). If  
 331 the penetration electric field were the main cause of the EEJ variations, we would ex-  
 332 pect to see strong correlations between the IEF and  $\Delta H$  in both longitude sectors. Quan-  
 333 titatively, the Pearson correlations between IEF and the deviations of  $\Delta H$  from the monthly  
 334 mean, (blue lines minus solid black lines in Figure 3), between 8 and 16 hr local time is  
 335  $-0.02$  for Peru (13 to 22 UT) and  $0.35$  for Brazil (11 to 20 UT). However, the fluctua-  
 336 tions observed in IEF appear to correlate with 1-hour-scale fluctuations observed at both  
 337 ground-based sites simultaneously (e.g., positive excursions at 15 UT and 17 UT, and  
 338 possibly at 13.5 UT). After filtering  $\Delta H$  and IEF to remove their 100-minute running  
 339 mean, the correlation increased to  $0.60$  (Peru) and  $0.61$  (Brazil). Thus, it is likely that  
 340 the 1-hour-scale fluctuations are caused in part by the penetration electric field, but the  
 341 larger, longer perturbations of interest here are not. Because of this, and because of the  
 342 consistency between the EEJ signatures and the neutral wind signatures, as discussed

343 above, we rule out the penetration electric field as the main cause of the extreme east-  
344 ward and westward EEJ observed by Swarm.

345 With neutral winds established as the causative mechanism, it is important to rule  
346 out geomagnetic activity as the cause of the extreme winds seen in Figure 2(c,d). It is  
347 well known that the EEJ can be reversed by the disturbance dynamo, a consequence of  
348 westward Coriolis forcing of neutral winds accelerated equatorward by auroral heating  
349 (Yamazaki & Maute, 2017). According to the modeling study by Huang et al. (2005),  
350 disturbance winds caused by a geomagnetic storm are mainly in the westward direction  
351 at middle and low latitudes. MIGHTI observations show both eastward and westward  
352 wind perturbations, which are different from the predicted pattern of the disturbance  
353 winds. Also, storm-driven wind perturbations are predicted to be much greater at F-region  
354 heights (above 150 km) than at E-region heights (below 150 km). MIGHTI observations  
355 show large wind perturbations below 150 km (including an eastward perturbation at 100  
356 km exceeding 100 m/s), which does not fit the classical picture of the disturbance winds.  
357 Furthermore, the westward disturbance wind at mid and low latitudes is stronger during  
358 nighttime than daytime. For instance, Xiong et al. (2015) showed that the average  
359 westward disturbance wind at 20–50° latitude is less than 50 m/s for  $K_p > 4$  at F-region  
360 heights during daytime, while it can exceed 100 m/s during nighttime. Thus, the geo-  
361 magnetic storm is unlikely to be the main cause of the extreme daytime winds detected  
362 by MIGHTI.

363 The simultaneous occurrence of the Lamb wave arrival, the EEJ signal, and the wind  
364 signal, combined with the lack of any significant wind or EEJ signals before this time,  
365 represents strong evidence to attribute the observed fluctuations to disturbances caused  
366 by the Tonga eruption. Nevertheless, it is possible that high-latitude heating launched  
367 traveling atmospheric disturbances during the recovery phase, and it is likely that the  
368 longer-term circulation changes caused by the storm have changed the background con-  
369 ditions upon which the Tonga signal is superimposed. It will be an interesting topic for  
370 future modeling and observational studies to elucidate the interplay of geomagnetic storm  
371 and volcanogenic effects on the thermosphere and ionosphere during this period.

## 372 4 Conclusion

373 The 15 Jan 2022 Tonga volcanic eruption caused extreme fluctuations in the iono-  
374 spheric wind dynamo, as observed by Swarm and ICON. On the leading part of the ini-  
375 tial disturbance, Swarm A observed an extreme (0.22 A/m) eastward EEJ at the 99.96th  
376 percentile of typical variability, while ICON-MIGHTI observed a strong westward wind  
377 in the Hall region and a strong eastward wind in the Pedersen region, a relationship con-  
378 sistent with recent theoretical and observational studies. Relative to typical variability,  
379 the wind perturbations (up to 200 m/s) were at or above the 99.9th percentile, and at  
380 some altitudes (e.g., ~140 km) were the strongest observed since ICON’s launch. On the  
381 trailing part of the initial disturbance, Swarm A observed the strongest westward EEJ  
382 (-0.17 A/m) of the mission, except for the 22-23 June 2015 geomagnetic storm, while ICON-  
383 MIGHTI observed eastward and westward winds in the Hall region and a westward wind  
384 in the Pedersen region, also at or above the 99.9th percentile.

385 The relationship between winds and EEJ is consistent with the theoretical and ob-  
386 servational relationships of neutral wind driving developed by Yamazaki et al. (2014) and  
387 Yamazaki et al. (2021). The westward electrojet in this case appears to be driven mostly  
388 by westward winds in the Pedersen region. Since the EEJ flows in the Hall region, this  
389 is a noteworthy example of nonlocal wind driving of the EEJ. The energy and current  
390 paths involved in this relationship would be an interesting topic for further study.

391 Initial reports on the ionosphere-thermosphere impacts of the Tonga eruption have  
392 focused on small- and meso-scale waves seen in TEC at amplitudes of at most a few TEC

units, as well as geomagnetic fluctuations 835 km away from and soon after the eruption. The MIGHTI and Swarm observations suggest that disturbances on larger spatial and temporal scales are equally, if not more consequential for the ionosphere-thermosphere system, even after  $\sim 10$  hours and  $\sim 10,000$  km of wave propagation. The extreme modifications of the ionospheric dynamo reported here are expected to have caused significant and observable redistributions of ionospheric plasma. As an example of an enormous impulse function, the Tonga eruption may be a useful test for atmosphere-ionosphere coupled models in extreme cases, and the ionospheric dynamo signatures reported here could be useful targets.

## Acknowledgments

The authors would like to recognize the work of the ICON and Swarm engineering and science teams. ICON is supported by NASA's Explorers Program through contracts NNG12FA45C and NNG12FA42I. The results presented in this paper rely on data collected at magnetic observatories. We thank the national institutes that support them and INTERMAGNET for promoting high standards of magnetic observatory practice ([www.intermagnet.org](http://www.intermagnet.org)). The authors thank Hermann Lühr, Claudia Stolle, Eileen McIver, and Jonathan Makela for fruitful scientific discussions and suggestions.

## Open Research

ICON data can be retrieved from the ICON website (<https://icon.ssl.berkeley.edu/Data>). The European Space Agency (ESA) is gratefully acknowledged for providing Swarm data, which is available from the Swarm website ([https://swarm-diss.esa.int/#swarm%2FLevel2daily%2Fentire\\_mission\\_data%2FEEF%2FTMS%2FSat\\_A](https://swarm-diss.esa.int/#swarm%2FLevel2daily%2Fentire_mission_data%2FEEF%2FTMS%2FSat_A)). The OMNI data were obtained from the GSFC/SPDF OMNIWeb interface at <https://omniweb.gsfc.nasa.gov>. Ground-based magnetometer data from HUA, TTB, and KOU are available from <https://intermagnet.org/data-donnee/download-eng.php>. Data from PIU is available from the LISN network ([http://lisn.igp.gob.pe/jdata/view/magnetometer/minute/piur/?itype=magnetometer&dtype=minute&daterange=2022%2F01%2F15+-+2022%2F01%2F15&networks=on&N\\_IGP=on&N\\_LISN=on&N\\_MAGDAS=on&countries=on&C\\_Argentina=on&C\\_Brasil=on&C\\_Colombia=on&C\\_Peru=on&stations=on&S\\_areq=on&S\\_leon=on&S\\_cuib=on&S\\_dejp=on&S\\_huan=on&S\\_jica=on&S\\_ancm=on&S\\_huam=on&S\\_icam=on&S\\_nazc=on&S\\_piur=on&bt\\_view=piur&S\\_saol=on&S\\_tara=on](http://lisn.igp.gob.pe/jdata/view/magnetometer/minute/piur/?itype=magnetometer&dtype=minute&daterange=2022%2F01%2F15+-+2022%2F01%2F15&networks=on&N_IGP=on&N_LISN=on&N_MAGDAS=on&countries=on&C_Argentina=on&C_Brasil=on&C_Colombia=on&C_Peru=on&stations=on&S_areq=on&S_leon=on&S_cuib=on&S_dejp=on&S_huan=on&S_jica=on&S_ancm=on&S_huam=on&S_icam=on&S_nazc=on&S_piur=on&bt_view=piur&S_saol=on&S_tara=on)).

## References

- Adam, D. (2022). Tonga volcano eruption created puzzling ripples in Earth's atmosphere. *Nature*, *601*, 497. Retrieved from <https://www.nature.com/articles/d41586-022-00127-1> doi: 10.1038/d41586-022-00127-1
- Alken, P. (2020). Estimating currents and electric fields at low latitudes from satellite magnetic measurements. In M. W. Dunlop & H. Lühr (Eds.), *Ionospheric multi-spacecraft analysis tools: Approaches for deriving ionospheric parameters* (pp. 233–254). Cham: Springer International Publishing. Retrieved from [https://doi.org/10.1007/978-3-030-26732-2\\_11](https://doi.org/10.1007/978-3-030-26732-2_11) doi: 10.1007/978-3-030-26732-2\_11
- Alken, P., Maus, S., Chulliat, A., Vigneron, P., Sirol, O., & Hulot, G. (2015). Swarm equatorial electric field chain: First results. *Geophysical Research Letters*, *42*(3), 673–680. doi: 10.1002/2014GL062658
- Alken, P., Maus, S., Vigneron, P., Sirol, O., & Hulot, G. (2013). Swarm SCARF equatorial electric field inversion chain. *Earth, Planets and Space*, *65*(11), 1309–1317. doi: 10.5047/eps.2013.09.008
- Anderson, D., Anghel, A., Chau, J., & Veliz, O. (2004). Daytime vertical  $E \times B$  drift velocities inferred from ground-based magnetometer observations at low

- latitudes . *Space Weather*, 2(11), n/a-n/a. doi: 10.1029/2004sw000095
- 442 Aryal, S., Evans, J. S., Correia, J., Burns, A. G., Wang, W., Solomon, S. C., . . .  
 443 Jee, G. (2020). First Global-Scale Synoptic Imaging of Solar Eclipse Effects in  
 444 the Thermosphere. *Journal of Geophysical Research: Space Physics*, 125(9).  
 445 doi: 10.1029/2020JA027789
- 446 Astafyeva, E. (2019). Ionospheric Detection of Natural Hazards. *Reviews of Geo-*  
 447 *physics*, 57(4), 1265–1288. doi: 10.1029/2019RG000668
- 448 Bretherton, F. P. (1969, 10). Lamb waves in a nearly isothermal atmosphere. *Quar-*  
 449 *terly Journal of the Royal Meteorological Society*, 95(406), 754–757. Retrieved  
 450 from <https://onlinelibrary.wiley.com/doi/10.1002/qj.49709540608>  
 451 doi: 10.1002/qj.49709540608
- 452 Duncombe, J. (2022). *The surprising reach of tonga’s giant atmospheric waves*. Re-  
 453 trieved 21 January 2022, from <https://doi.org/10.1029/2022E0220050>
- 454 Englert, C. R., Harlander, J. M., Brown, C. M., Marr, K. D., Miller, I. J., Stump,  
 455 J. E., . . . Immel, T. J. (2017). Michelson Interferometer for Global High-  
 456 Resolution Thermospheric Imaging (MIGHTI): Instrument Design and Cali-  
 457 bration. *Space Science Reviews*, 212(1-2), 553–584. Retrieved from [http://](http://dx.doi.org/10.1007/s11214-017-0358-4)  
 458 [dx.doi.org/10.1007/s11214-017-0358-4](http://dx.doi.org/10.1007/s11214-017-0358-4) [http://link.springer.com/](http://link.springer.com/10.1007/s11214-017-0358-4)  
 459 [10.1007/s11214-017-0358-4](http://link.springer.com/10.1007/s11214-017-0358-4) doi: 10.1007/s11214-017-0358-4
- 460 Finlay, C. C., Kloss, C., Olsen, N., Hammer, M. D., Tøffner-Clausen, L., Grayver,  
 461 A., & Kuvshinov, A. (2020). The CHAOS-7 geomagnetic field model and  
 462 observed changes in the South Atlantic Anomaly. *Earth, Planets and Space*,  
 463 72(1), 1–31.
- 464 Harding, B. J., Chau, J. L., He, M., Englert, C. R., Harlander, J. M., Marr, K. D.,  
 465 . . . Immel, T. J. (2021). Validation of ICON-MIGHTI Thermospheric Wind  
 466 Observations: 2. Green-Line Comparisons to Specular Meteor Radars. *Jour-*  
 467 *nal of Geophysical Research: Space Physics*, 126(3), 1–12. Retrieved from  
 468 <https://onlinelibrary.wiley.com/doi/10.1029/2020JA028947> doi:  
 469 10.1029/2020JA028947
- 470 Harding, B. J., Makela, J. J., Englert, C. R., Marr, K. D., Harlander, J. M., Eng-  
 471 land, S. L., & Immel, T. J. (2017). The MIGHTI Wind Retrieval Al-  
 472 gorithm: Description and Verification. *Space Science Reviews*, 212(1-  
 473 2), 585–600. Retrieved from [http://dx.doi.org/10.1007/s11214-017-](http://dx.doi.org/10.1007/s11214-017-0359-3)  
 474 [0359-3](http://dx.doi.org/10.1007/s11214-017-0359-3) <http://link.springer.com/10.1007/s11214-017-0359-3> doi:  
 475 10.1007/s11214-017-0359-3
- 476 Huang, C.-M., Richmond, A., & Chen, M.-Q. (2005). Theoretical effects of geomag-  
 477 netic activity on low-latitude ionospheric electric fields. *Journal of Geophysical*  
 478 *Research: Space Physics*, 110(A5).
- 479 Immel, T. J., England, S. L., Mende, S. B., Heelis, R. A., Englert, C. R., Edelstein,  
 480 J., . . . Sirk, M. M. (2018). The Ionospheric Connection Explorer Mission:  
 481 Mission Goals and Design. *Space Science Reviews*, 214(1), 13. Retrieved from  
 482 <http://dx.doi.org/10.1007/s11214-017-0449-2> [http://link.springer](http://link.springer.com/10.1007/s11214-017-0449-2)  
 483 [.com/10.1007/s11214-017-0449-2](http://link.springer.com/10.1007/s11214-017-0449-2) doi: 10.1007/s11214-017-0449-2
- 484 Inchin, P. A., Heale, C. J., Snively, J. B., & Zettergren, M. D. (2020). The Dynam-  
 485 ics of Nonlinear Atmospheric Acoustic-Gravity Waves Generated by Tsunamis  
 486 Over Realistic Bathymetry. *Journal of Geophysical Research: Space Physics*,  
 487 125(12), 1–18. doi: 10.1029/2020JA028309
- 488 Inchin, P. A., Snively, J. B., Zettergren, M. D., Komjathy, A., Verkhoglyadova,  
 489 O. P., & Tulasi Ram, S. (2020). Modeling of Ionospheric Responses to Atmo-  
 490 spheric Acoustic and Gravity Waves Driven by the 2015 Nepal Mw7.8 Gorkha  
 491 Earthquake. *Journal of Geophysical Research: Space Physics*, 125(4). doi:  
 492 10.1029/2019JA027200
- 493 Jet Propulsion Laboratory. (2022). *Tonga eruption sent ripples through earth’s iono-*  
 494 *sphere*. Retrieved 20 Feb 2022, from [https://www.jpl.nasa.gov/news/tonga](https://www.jpl.nasa.gov/news/tonga-eruption-sent-ripples-through-earths-ionosphere)  
 495 [-eruption-sent-ripples-through-earths-ionosphere](https://www.jpl.nasa.gov/news/tonga-eruption-sent-ripples-through-earths-ionosphere)

- 497 King, J. H., & Papitashvili, N. E. (2005). Solar wind spatial scales in and  
498 comparisons of hourly Wind and ACE plasma and magnetic field data.  
499 *Journal of Geophysical Research: Space Physics*, *110*(A2), 1–9. doi:  
500 10.1029/2004JA010649
- 501 Li, R., Lei, J., & Dang, T. (2021). The Solar Eclipse Effects on the Up-  
502 per Thermosphere. *Geophysical Research Letters*, *48*(15), 1–10. doi:  
503 10.1029/2021GL094749
- 504 Lin, J.-T., Rajesh, P. K., Lin, C. C. H., Chou, M.-Y., Liu, J.-Y., Yue, J., . . . Kung,  
505 M.-M. (2022). Rapid conjugate appearance of the giant ionospheric lamb wave  
506 in the northern hemisphere after hunga-tonga volcano eruptions. *Earth and*  
507 *Space Science Open Archive*, *27*. Retrieved from [https://doi.org/10.1002/](https://doi.org/10.1002/essoar.10510440.2)  
508 [essoar.10510440.2](https://doi.org/10.1002/essoar.10510440.2) doi: 10.1002/essoar.10510440.2
- 509 Makela, J. J., Baughman, M., Navarro, L. A., Harding, B. J., Englert, C. R., Har-  
510 lander, J. M., . . . Immel, T. J. (2021). Validation of ICON-MIGHTI Thermo-  
511 spheric Wind Observations: 1. Nighttime Red-Line Ground-Based Fabry-Perot  
512 Interferometers. *Journal of Geophysical Research: Space Physics*, *126*(2),  
513 1–29. Retrieved from [https://onlinelibrary.wiley.com/doi/10.1029/](https://onlinelibrary.wiley.com/doi/10.1029/2020JA028726)  
514 [2020JA028726](https://onlinelibrary.wiley.com/doi/10.1029/2020JA028726) doi: 10.1029/2020JA028726
- 515 Manoj, C., Maus, S., Lühr, H., & Alken, P. (2008). Penetration character-  
516 istics of the interplanetary electric field to the daytime equatorial iono-  
517 sphere. *Journal of Geophysical Research: Space Physics*, *113*(12), 1–11. doi:  
518 10.1029/2008JA013381
- 519 Nishida, K., Kobayashi, N., & Fukao, Y. (2014, 1). Background Lamb waves in  
520 the Earth’s atmosphere. *Geophysical Journal International*, *196*(1), 312–316.  
521 Retrieved from <https://academic.oup.com/gji/article/196/1/312/594635>  
522 doi: 10.1093/gji/ggt413
- 523 Richmond, A. D. (1973). Equatorial electrojet-I. Development of a model including  
524 winds and instabilities. *Journal of Atmospheric and Terrestrial Physics*, *35*(6),  
525 1083–1103. doi: 10.1016/0021-9169(73)90007-X
- 526 Soares, G., Yamazaki, Y., & Matzka, J. (2022). Localized geomagnetic disturbance  
527 due to ionospheric response to the hunga tonga eruption on january 15, 2022.  
528 *Earth and Space Science Open Archive*, *12*. Retrieved from [https://doi.org/](https://doi.org/10.1002/essoar.10510482.1)  
529 [10.1002/essoar.10510482.1](https://doi.org/10.1002/essoar.10510482.1) doi: 10.1002/essoar.10510482.1
- 530 Themens, D. R., Watson, C., Žagar, N., Vasylykevych, S., Elvidge, S., Mccaffrey,  
531 A., . . . Jayachandran, P. T. (2022). Global propagation of ionospheric  
532 disturbances associated with the 2022 tonga volcanic eruption. *Earth and*  
533 *Space Science Open Archive*, *25*. Retrieved from [https://doi.org/10.1002/](https://doi.org/10.1002/essoar.10510350.1)  
534 [essoar.10510350.1](https://doi.org/10.1002/essoar.10510350.1) doi: 10.1002/essoar.10510350.1
- 535 Xiong, C., Lühr, H., & Fejer, B. G. (2015). Global features of the disturbance winds  
536 during storm time deduced from CHAMP observations. *Journal of Geophysical*  
537 *Research A: Space Physics*, *120*(6), 5137–5150. doi: 10.1002/2015JA021302
- 538 Yamazaki, Y., Harding, B. J., Stolle, C., & Matzka, J. (2021). Neutral Wind Profiles  
539 During Periods of Eastward and Westward Equatorial Electrojet. *Geophysical*  
540 *Research Letters*, *48*(11), 1–10. doi: 10.1029/2021GL093567
- 541 Yamazaki, Y., & Maute, A. (2017). Sq and EEJ—A Review on the Daily Varia-  
542 tion of the Geomagnetic Field Caused by Ionospheric Dynamo Currents. *Space*  
543 *Science Reviews*, *206*(1-4), 299–405. Retrieved from [http://dx.doi.org/10](http://dx.doi.org/10.1007/s11214-016-0282-z)  
544 [.1007/s11214-016-0282-z](http://dx.doi.org/10.1007/s11214-016-0282-z) doi: 10.1007/s11214-016-0282-z
- 545 Yamazaki, Y., Richmond, A. D., Maute, A., Liu, H.-L., Pedatella, N., & Sassi, F.  
546 (2014). On the day-to-day variation of the equatorial electrojet during quiet  
547 periods. *Journal of Geophysical Research: Space Physics*, *119*(8), 6966–  
548 6980. Retrieved from <http://doi.wiley.com/10.1002/2014JA020243> doi:  
549 10.1002/2014JA020243
- 550 Zettergren, M. D., & Snively, J. B. (2019). Latitude and Longitude Dependence of  
551 Ionospheric TEC and Magnetic Perturbations From Infrasonic-Acoustic Waves

552           Generated by Strong Seismic Events.           *Geophysical Research Letters*, 46(3),  
553           1132–1140. doi: 10.1029/2018GL081569  
554       Zhang, S.-R., Vierinen, J., Aa, E., Goncharenko, L., Erickson, P., Rideout, W., . . .  
555           Spicher, A. (2022). 2022 tonga volcanic eruption induced global propagation  
556           of ionospheric disturbances via lamb waves.           *Earth and Space Science Open*  
557           *Archive*, 15. Retrieved from <https://doi.org/10.1002/essoar.10510445.1>  
558           doi: 10.1002/essoar.10510445.1

Figure 1.

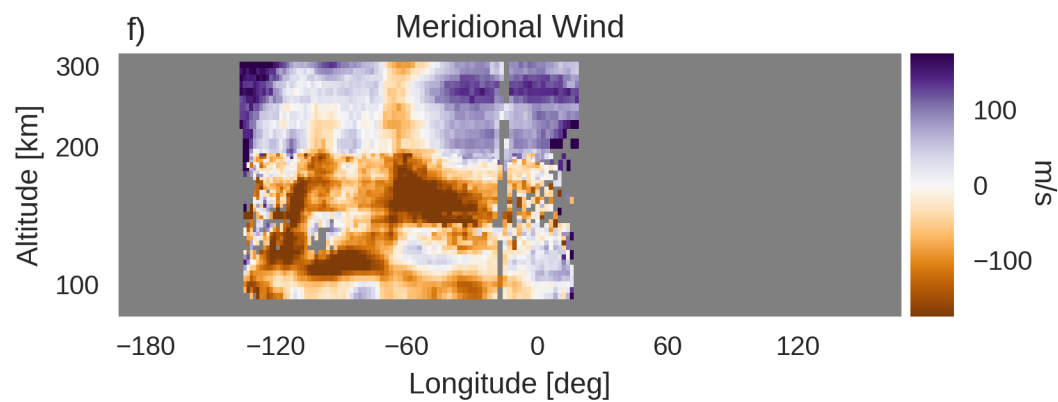
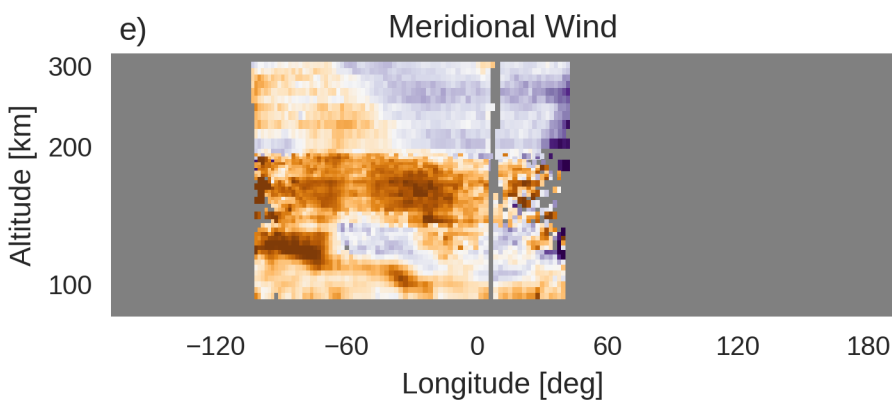
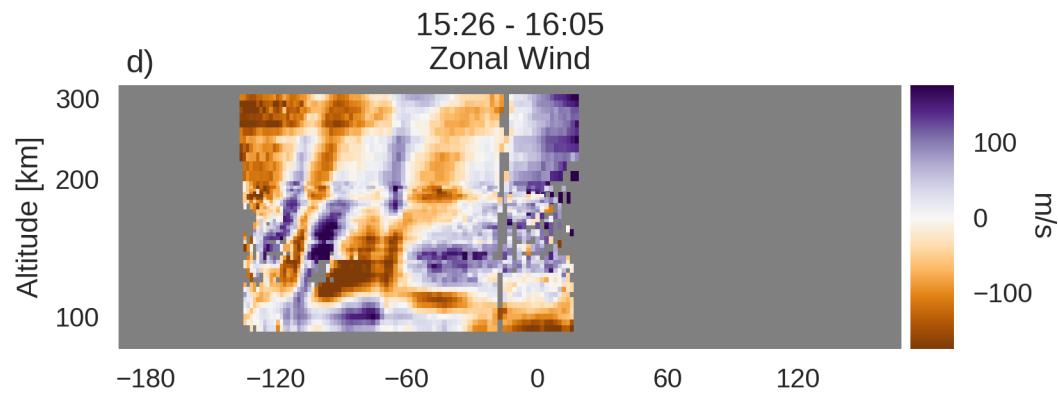
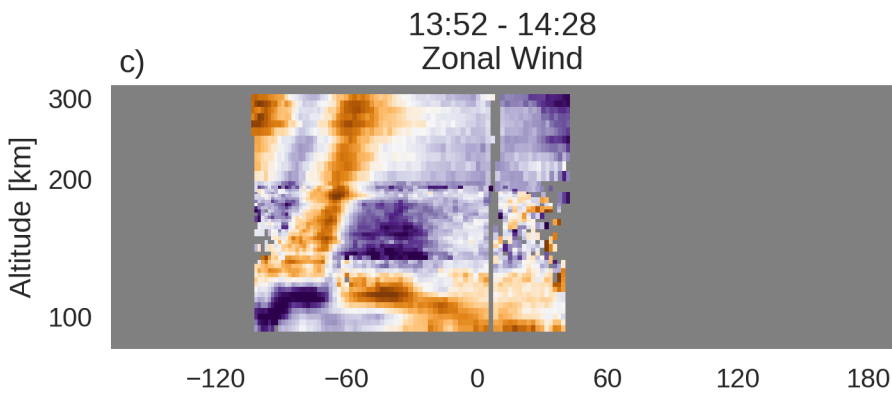
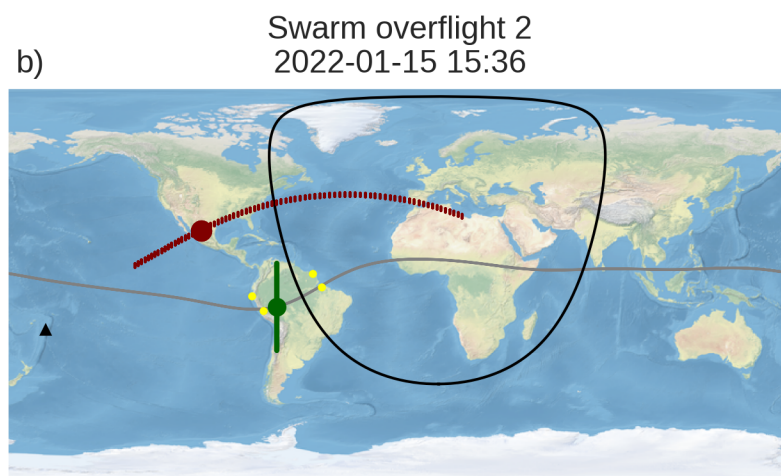
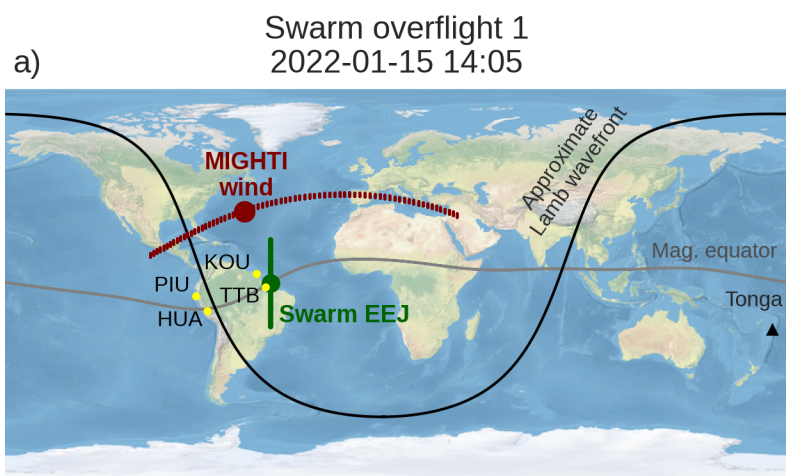
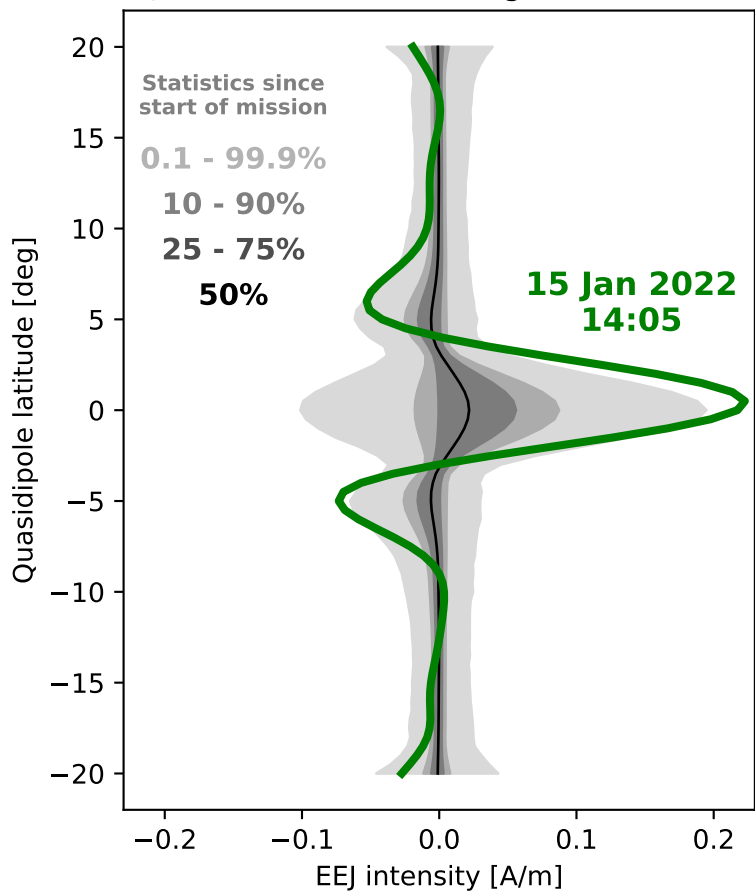
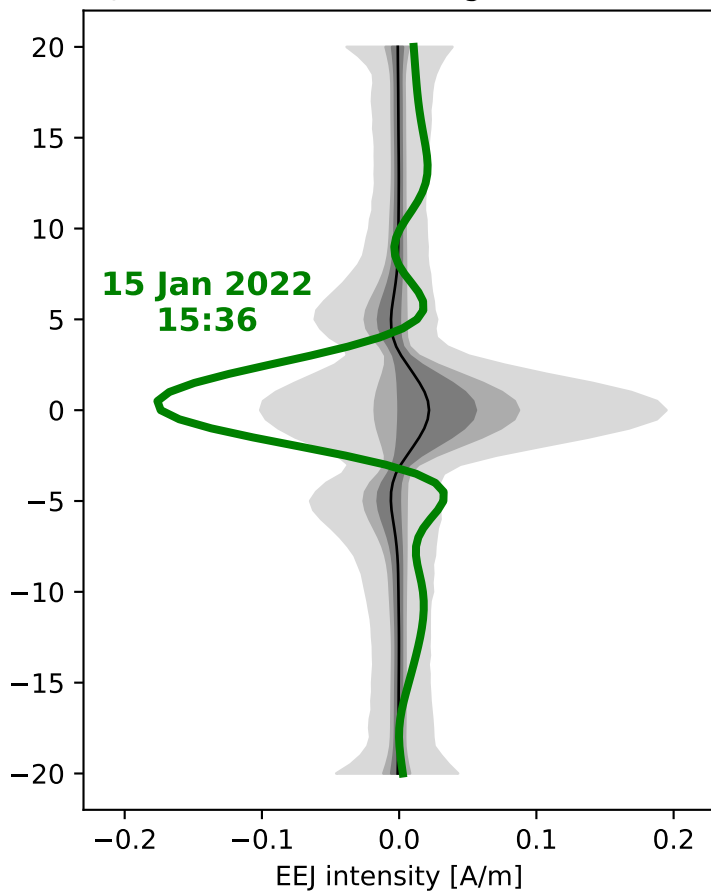


Figure 2.

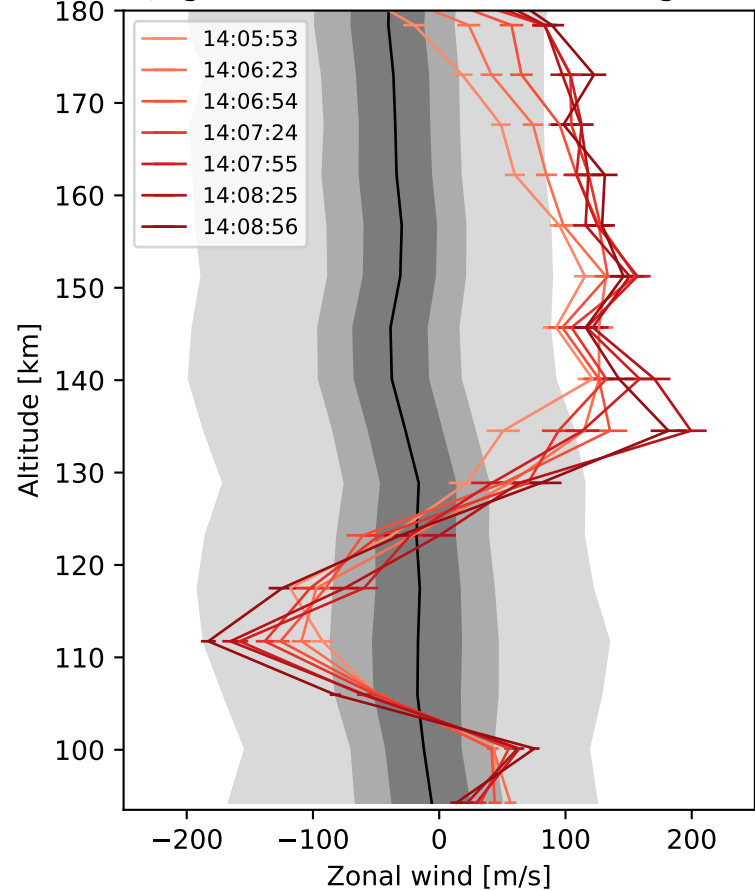
a) Swarm overflight 1



b) Swarm overflight 2



c) MIGHTI wind profiles at same great-circle distance from Tonga



d) MIGHTI wind profiles at same great-circle distance from Tonga

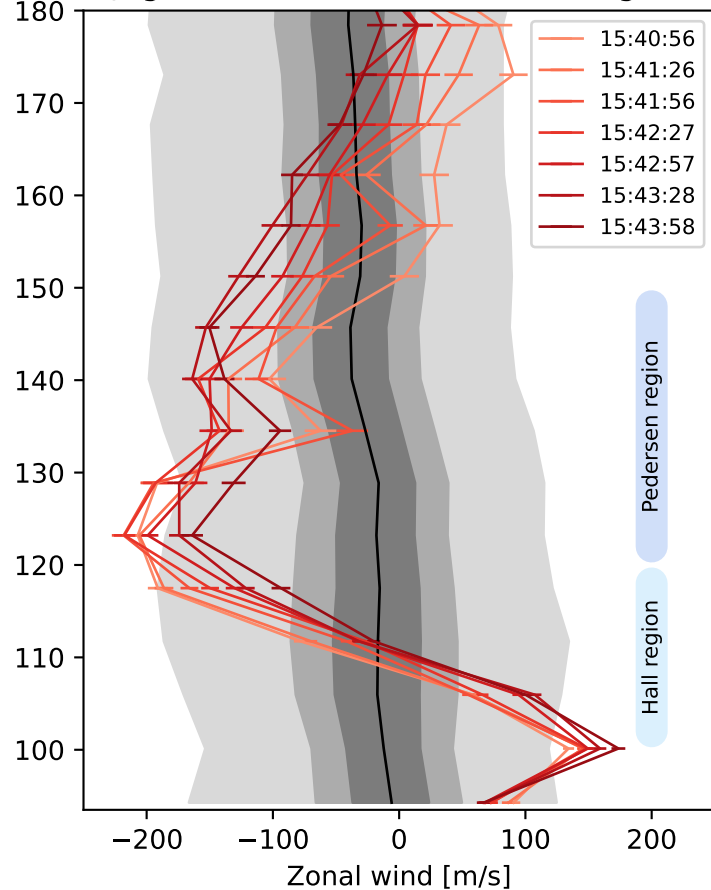


Figure 3.

